

See discussions, stats, and author profiles for this publication at:  
<https://www.researchgate.net/publication/12165771>

# Raman spectroscopy in magnetic fluids. Biomol Eng

ARTICLE *in* BIOMOLECULAR ENGINEERING · FEBRUARY 2001

Impact Factor: 3.17 · DOI: 10.1016/S1389-0344(00)00064-2 · Source: PubMed

CITATIONS

23

READS

37

4 AUTHORS, INCLUDING:



P. C. Morais

University of Brasília

437 PUBLICATIONS 4,498 CITATIONS

SEE PROFILE



Sebastião W da Silva

University of Brasília

103 PUBLICATIONS 967 CITATIONS

SEE PROFILE

## Raman spectroscopy in magnetic fluids

Paulo Cesar Morais <sup>a,\*</sup>, Sebastião William da Silva <sup>a</sup>, Maria Aparecida Godoy Soler <sup>a</sup>,  
Norbert Buske <sup>b</sup>

<sup>a</sup> Instituto de Física, Núcleo de Física Aplicada, Universidade de Brasília, C.P. 04455, CEP 70919-970 Brasília-DF, Brazil

<sup>b</sup> Mediport Kardiotechnik GmbH, Wiesenweg 10, D-12247 Berlin, Germany

Received 17 March 2000; received in revised form 10 May 2000; accepted 10 May 2000

### Abstract

In this work Raman spectroscopy was used to investigate uncoated magnetic fluids (UMF's) and coated magnetic fluids (CMF's). The coating agents were *N*-oleoylsarcosine, dodecanoic acid, and ethoxylated polyalcohol. The Raman probe is the hydroxyl (OH) group chemisorbed at the magnetic nanoparticle surface and the measurements were performed in the typical OH bending and OH stretching regions. The room temperature Raman data obtained from the UMF's and CMF's are compared to each other and with the data obtained from liquid water. Suppression of Raman modes from the MF's are discussed in terms of symmetry reduction and in terms of the interaction between the chemisorbed OH-group and the surrounding medium. The relative grafting coefficient associated to different coatings are estimated from the Raman data. The highest grafting coefficient is achieved with a single coating of dodecanoic acid in the hydrocarbon-based MF. The surface-grafting coefficient of the *N*-oleoylsarcosine-coated MF reduces when the polar liquid carrier replaces the non-polar liquid carrier. In comparison to liquid water, it was found that the hydrogen bonding between the chemisorbed OH-group and the solvent was enhanced in UMF's and reduced in CMF's. © 2001 Elsevier Science B.V. All rights reserved.

**Keywords:** Magnetic fluids; Raman spectroscopy; Hydrogen bonding; Grafting coefficient

### 1. Introduction

Magnetic fluids (MF's) are ultra-stable colloidal systems consisting of monodomain magnetic nanoparticles dispersed in organic or inorganic liquid carrier [1]. In ionic MF's the colloidal stability is mainly achieved through the electrostatic repulsion among the positively or negatively charged nanoparticles [2]. In this case the surface charge density and the ionic strength of the medium need to be precisely controlled in such a way that repulsion does overcome the magnetic dipolar attraction that favors nanoparticle flocculation. In the usual ionic ferrite-based MF's low pH aqueous medium sets in a positive charge density, due to proton transfer from the medium to the nanoparticle surface. By contrast, negative surface charge density is obtained at high pH values as a result of the proton transfer from the nanoparticle surface out to the aqueous medium, thus

leaving behind negatively charged oxygen atoms in the nanoparticle surface. A microscopic model for the pH-dependent surface charge-discharge process in metal oxide-based ionic MF's involves the proton tunneling across a strongly bonded water layer around the nanoparticle surface [3]. In coated MF's, however, surface-coated nanoparticles maintain colloidal stability, once steric repulsion among the coated magnetic nanoparticles has overcome the magnetic dipolar attraction [4]. The outer ends of the surface molecular coating in coated MF's may be either polar or non-polar, thus resulting for instance, in stable aqueous-based MF's or stable hydrocarbon-based MF's, respectively. In addition to the nanoparticle electrostatic repulsion and dipolar attraction the thermal energy and the Van der Waals interaction also play an important role in the magnetic colloidal stability. Thermal energy favors colloidal stability by taking magnetic nanoparticles apart while Van der Waals interaction stick nanoparticles together. Finally, electrostatic plus steric repulsion may work together against nanoparticle clustering in a new

\* Corresponding author. Tel.: +55-61-2736655; fax: +55-61-2723151.

E-mail address: pcmor@fis.unb.br (P.C. Morais).

class of water-based MF's. The most striking aspect of this third class of MF's is the possibility that colloidal stability may be achieved at physiological pH and physiological salinity. Adding non-toxicity to the two previous features (pH and salinity) one has the basic characteristics of the biocompatible magnetic fluids (BMF's) [5,6].

Biological specificity may be brought into the BMF's, once a wide variety of bioactive molecules can be used to perform an extra coating on top of the first coating layer (pre-coating) of the magnetic nanoparticles [7]. To meet a particular biological application the pre-coated nanoparticle surface needs to be engineered to efficiently link more complex structures such as nucleotides, oligonucleotides, peptides, vitamins, antibiotics, and antibodies, among others. Separation and purification of cells [8], drug delivery systems [9], contrast agents for magnetic resonance imaging [10], and hyperthermia of biological tissues applied to tumor therapy [11] are just a few examples of the many possibilities of applications of BMF's in biology and medical diagnosis and therapy. Notice that in the biotechnological applications one seeks to achieve the highest molecular specificity associated to the ideal grafting coefficient, as a way to achieve the maximum efficiency in the desired application. However, as far as the molecular engineering of the nanoparticle surface is concerned, it is quite obvious that the physicochemical properties of the molecular layer chemisorbed at the nanoparticle surface play a key role, though little has been done to investigate its structure and interaction with the surrounding medium. The biological specificity and the grafting coefficient of a particular bioactive molecule depend upon the efficiency of the link between the nanoparticle surface and the coating structure. Here, the grafting coefficient associated to molecular species ( $\xi$ ), with respect to a given surface, means the surface concentration (in units of mol/cm<sup>2</sup>) of that particular molecular structure bonding at the surface. Typical values for the grafting coefficient are on the order of 10<sup>-10</sup> mol/cm<sup>2</sup> [12]. From now on the ionic MF's will be referred to as uncoated magnetic fluids (UMF's), in contrast with the pre-coated MF's that will be named as coated magnetic fluids (CMF's).

The traditional techniques used in the investigation of MF's are the high-resolution microscopy [13], X-ray diffraction [14], static magnetic birefringence [15], and magnetometry [16]. More recently, magnetic resonance has been introduced as a valuable tool in the investigation of several properties of MF's [17]. The resonant center used in the investigation of MF's is either the magnetic nanoparticle itself [18] or a paramagnetic probe intentionally introduced as a dopant in the carrier fluid [19]. Effects of particle concentration [20], ionic strength [21], particle size and temperature [22] have been investigated using the nanoparticle itself as

the resonant probe. Particle size polydispersity determination [19] as well as investigation of the ionic layer thickness around the magnetic nanoparticles [23] in low-pH UMF's used the [Cu(H<sub>2</sub>O)<sub>6</sub>]<sup>2+</sup> dopant as the paramagnetic probe. Despite the possibility of using magnetic resonance in the investigation of the charge-discharge process in UMF's [21], microscopic information concerning the proton transfer across the water-based layer surrounding the magnetic nanoparticle seems to be hardly obtained from X-band experiments.

Neither the traditional magnetization measurements nor the unconventional magnetic resonance would be of great help to monitor the molecular layer chemisorbed at the nanoparticle surface in MF's, though this is a fundamental issue in the molecular engineering of BMF's for specific targeting. In contrast, Raman spectroscopy emerges as a promising and powerful technique to investigate qualitatively as well as quantitatively surface chemisorbed species. In previous works we have studied interactions of the molecular layer chemisorbed at the nanoparticle surface of copper and zinc-ferrite UMF's [24]. The single CMF based on dodecanoic acid (first coating) and diluted in hydrocarbon and the double CMF based on dodecanoic acid (first coating) following an ethoxylated polyalcohol (second coating) and peptized in water, were recently investigated using Raman spectroscopy [25]. In this work, we have used Raman spectroscopy to study some of the properties of the molecular layer chemisorbed at the surface of magnetic nanoparticles of UMF's and CMF's based on different spinel ferrites, coated with different molecular species, and dispersed in water and hydrocarbon. Comparison between the Raman spectra obtained from liquid water and the Raman spectra obtained from the UMF's and CMF's provide a useful way to estimate the effective grafting coefficient associated to the molecular species chemisorbed at the nanoparticle surface. This is obtained by looking at the OH bending and OH stretching Raman modes of the OH-group chemisorbed at the nanoparticle surface. In addition, the Raman data also provide a straightforward way to determine the enthalpy change associated to the hydrogen bonding strength involving the hydroxyl-group chemisorbed at the nanoparticle surface and the surrounding medium.

This paper is organized as follows. A brief description of the process of preparation of UMF's and CMF's as well as the description of the Raman setup is given in Section 2. Section 3 is divided into three sub-sections in which the Raman data related to liquid water (Section 3.1), UMF's (Section 3.2) and CMF's (Section 3.3) are presented and discussed. Conclusions are given in Section 4.

## 2. Experimental

The UMF samples used in this work were prepared by the chemical condensation method of aqueous iron, copper, zinc, nickel, and manganese cations in alkaline medium, following passivation of the nanoparticle surface and peptization of the nanoparticles in water at pH around 3 [2]. The CMF samples were obtained by chemical co-precipitation of Fe (II) and Fe (III) ions in alkaline medium to produce magnetite nanoparticles, following treatment with different coatings and peptization in hydrocarbon and aqueous medium. Three coating agents were used in the production of the magnetite-based CMF samples, namely, *N*-oleoylsarcosine, dodecanoic acid, and an ethoxylated polyalcohol. The *N*-oleoylsarcosine magnetite-coated nanoparticles were peptized in both aqueous and hydrocarbon media to yield two CMF samples. A single coating of the magnetite nanoparticles using dodecanoic acid yields stable CMF samples in hydrocarbon medium. Finally, a double coating of the magnetite nanoparticles, firstly with dodecanoic acid and secondly with an ethoxylated polyalcohol yields stable CMF samples in aqueous medium [26].

The Raman setup consists of a double 0.85 m 1401 Spex monochromator equipped with a water-cooled Gallium Arsenide Hamamatsu photomultiplier tube and a SR400 model photocounting system. The samples (UMF's and CMF's) used to obtain the Raman data were diluted to about  $2 \times 10^{16}$  particle/cm<sup>3</sup>. The 514 nm line from an Argon ion laser was used to illuminate the MF samples, at an optical power of the order of 150 mW outside the sample holder. The laser beam passes vertically through the sample holder, i.e. parallel to the spectrometer entrance slit. The scattered light is collected from a small rectangular area of about 1/2 mm wide  $\times$  1 mm high. All the Raman measurements (liquid water and MF samples) were performed at room temperature, for the typical intra-molecular OH bending (around 1600 cm<sup>-1</sup>) and OH stretching (around 3500 cm<sup>-1</sup>) mode regions.

## 3. Results and discussions

The UMF and CMF Raman data presented and discussed here are focused on the OH bending and OH stretching Raman modes of the hydroxyl-group chemisorbed at the nanoparticle surface. Comparison between the Raman data obtained from liquid water and from the MF samples, in both bending and stretching regions, will be used to discuss the following aspects observed in the uncoated magnetic fluid (UMF) and the coated magnetic fluids (CMF) data. First, the quenching of Raman lines observed in the MF samples. Second, to explain the Raman shift observed in the OH

bending and OH stretching Raman modes associated to the UMF samples. Third, to calculate the enthalpy change associated to the hydrogen bonding strength involving the chemisorbed OH-group. Fourth, to estimate the relative grafting coefficient associated to the coating species.

### 3.1. Liquid water

Raman spectroscopy is probably the most important technique used to obtain information concerning to the intra- and inter-molecular vibrational modes of liquid water [27,28]. Numerical analysis based on gaussian-shaped Raman modes has indicated that liquid water may have as many as seven fundamental intra-molecular vibrational distributions and nine inter-molecular vibrational distributions, depending upon the specific scheme used in the analysis and designation of the Raman modes [27–30]. Here, vibrational distributions mean that all Raman modes are inhomogeneously broadened, i.e. the bond lengths and the bond angles are widely distributed due to molecular interactions. Within the framework of the tetrahedral bonded structure for liquid water it has been shown that there are two different bending distributions and as many as six stretching distributions [27]. The OH bending Raman feature, near 1640 cm<sup>-1</sup> for liquid water, has been found to be a convolution of two distinct gaussian components. Such a bending components have previously been thought to arise from different levels of hydrogen bonding [31]. The gaussian feature at the higher frequency side of the spectrum ( $\nu_2'$ ) peaks around 1643 cm<sup>-1</sup> and may correspond to the non-hydrogen bonding water. A second gaussian bending component ( $\nu_2$ ) near 1545 cm<sup>-1</sup> presumably corresponds to water molecule engaged in a fully hydrogen bonding configuration. The two gaussian bending components (dashed lines in the left-hand side of Fig. 1) are obtained from our analysis of the liquid water Raman data. The Raman structure in the 3000–4000 cm<sup>-1</sup> regions corresponds to the OH stretching modes of liquid water, arising from the various amounts of hydrogen bonding. The two OH stretching Raman components (dashed lines in the right-hand side of Fig. 1) at the higher end frequency of the spectra ( $\nu^s$  and  $\nu^a$ ) describe non-hydrogen bonding modes (OH<sup>••••</sup>); with  $\nu^s$  representing the symmetric stretching mode while  $\nu^a$  represents the anti-symmetric stretching mode. In contrast, the four Raman components ( $\nu_d^s$ ,  $\nu_d^a$ ,  $\nu_b$  and  $\nu_w$ ) at lower frequencies (dashed lines in the right-hand side of Fig. 1) describe hydrogen-bonding modes (OH<sup>••••</sup>).  $\nu_d^s$  and  $\nu_d^a$  refer to symmetrically hydrogen bonding modes, while  $\nu_b$  refers to the anti-symmetric hydrogen bonding mode [27,28]. It has been shown that the Raman intensity of the  $\nu_w$  mode is very low compared to the other OH stretching Raman modes and thus only five modes

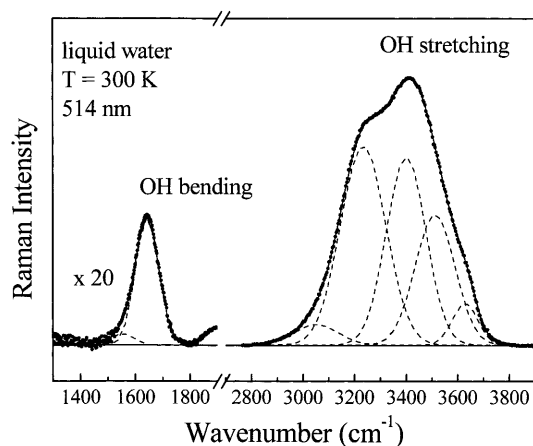


Fig. 1. Raman spectrum of liquid water in the OH bending region (left-hand side) and in the OH stretching region (right-hand side). Symbols are experimental data, solid lines represent the best numerical fit, and dashed lines represent the gaussian-shaped Raman modes.

instead of six are used to fit the experimental data in liquid water [27]. Symbols in Fig. 1 show the room temperature Raman spectra of liquid water, in the OH bending (left-hand side) and OH stretching (right-hand side) mode regions. The solid lines going through the symbols in Fig. 1 represent the best fit of the experimental data using gaussian-shaped components, while the dashed and dotted lines represent each Raman mode individually, according to our fitting procedure. The hydrogen bonding OH bending ( $\nu_2$ ), non-hydrogen bonding OH bending ( $\nu'_2$ ), symmetric hydrogen bonding OH stretching ( $\nu_d^s$ ), asymmetric hydrogen bonding OH stretching ( $\nu_d^a$ ), asymmetric partially bonding OH stretching ( $\nu_b$ ), symmetric non-hydrogen bonding ( $\nu^s$ ), and asymmetric non-hydrogen bonding ( $\nu^a$ ) Raman shifts were identified from the data available in reference [27] and are shown in Table 1.

A quantitative analysis of the hydrogen bonding strength or the enthalpy change ( $\Delta H$ ) can be performed using the van't Hoff equation [30]. The approximate

calculation is based on the liquid water equilibrium ( $\text{O}=\text{H}\cdots\text{O} \rightleftharpoons \text{O}=\text{H} + \text{O}$ ), to which is assigned an enthalpy of  $\Delta H = 2.53$  kcal/mol [28]. The liquid water equilibrium constant ( $K$ ) is given by the ratio  $K = A_B/A_U$ .  $A_B$  is the sum of the integrated gaussian Raman components related to the hydrogen bonding OH stretching modes.  $A_U$  is the sum of the integrated gaussian Raman components related to the non-hydrogen bonding OH stretching modes. The van't Hoff equation reads  $\ln K = A - \Delta H/RT$ , where  $R = 1.99$  cal/mol  $\times K$  is the gas constant,  $T$  is the absolute temperature, and  $A = -3.579$  is the intercept constant for liquid water [28]. Note that the higher the population of the hydrogen bonding modes with respect to the non-hydrogen bonding modes, the greater the enthalpy change. Though approximate, we assume the intercept constant for the MF samples equals to  $-3.579$ . Therefore, the hydrogen bonding strength can be estimated from the Raman data, as quoted in the last column of Table 1. The enthalpy change we found for liquid water ( $\Delta H = 2.74$  kcal/mol) is in very good agreement with the literature.

### 3.2. Uncoated magnetic fluids

Only low pH UMF samples have been analyzed here, i.e. samples containing surface proton-enriched magnetic nanoparticles. The Raman spectra in the typical intra-molecular OH bending and OH stretching mode regions taken from iron, copper, zinc, nickel, and manganese spinel ferrite-based diluted magnetic fluid samples are shown in Fig. 2 and Fig. 3, respectively. The solid lines in Fig. 2 represent the best fit of the Raman spectra of all samples corresponding to the intra-molecular OH bending modes, using gaussian-shaped curves. Dashed lines in Fig. 2 represent the individual OH bending modes according to our fitting procedure. Likewise, the solid lines in Fig. 3 represent the best fit of the Raman spectra of all samples corresponding to

Table 1  
Room temperature Raman data obtained from the best numerical fit of the spectra using gaussian-shaped curves

	Sample	Bending ( $\text{cm}^{-1}$ )		Stretching ( $\text{cm}^{-1}$ )					$\Delta H$ (kcal/mol)
		$\nu_2$	$\nu'_2$	$\nu_d^s$	$\nu_d^a$	$\nu_b$	$\nu^s$	$\nu^a$	
UMF	Liquid water	1545	1643	3051	3233	3399	3511	3628	2.74
	CuFe <sub>2</sub> O <sub>4</sub>	1524	1625	—	3257	3458	—	3622	3.66
	ZnFe <sub>2</sub> O <sub>4</sub>	1514	1624	—	3260	3470	—	3623	3.87
	NiFe <sub>2</sub> O <sub>4</sub>	1500	1616	—	3269	3479	—	3633	4.03
	MnFe <sub>2</sub> O <sub>4</sub>	1480	1611	—	3287	3483	—	3635	4.00
	Fe <sub>3</sub> O <sub>4</sub>	—	1610	—	3304	3493	—	3640	4.26
CMF	WBO	—	—	—	—	3658	—	3691	2.00
	WBD	—	—	—	—	3620	—	3683	2.38
	HBO	—	—	—	—	3619	—	3683	1.93
	HBS	—	—	—	—	—	—	3663	—

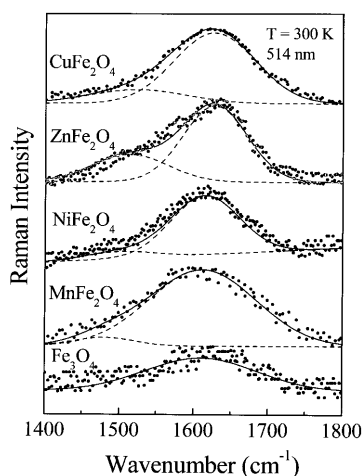


Fig. 2. Raman spectra of the UMF's in the OH bending region. Symbols are experimental data, solid lines represent the best numerical fit, and dashed lines represent the gaussian-shaped Raman modes.

the intra-molecular OH stretching modes, using gaussian-shaped curves. The individual OH stretching modes are shown separately in Fig. 3 through the dashed lines.

We first discuss the most striking result obtained from the analysis of the Raman data (see Table 1), namely, the suppression of all symmetric OH stretching modes from the UMF samples. The OH stretching band in the UMF samples is nicely fitted with only three Raman peaks instead of five Raman peaks as in liquid water. Though in liquid water the OH stretching mode at  $3051\text{ cm}^{-1}$  is just a shoulder, the OH stretching mode at  $3511\text{ cm}^{-1}$  is a quite intense peak. Thus, the suppression of the higher frequency symmetric OH stretching mode from the UMF Raman spectra is easily detected by any robust fitting procedure. This is strong evidence that the Raman spectra taken from UMF

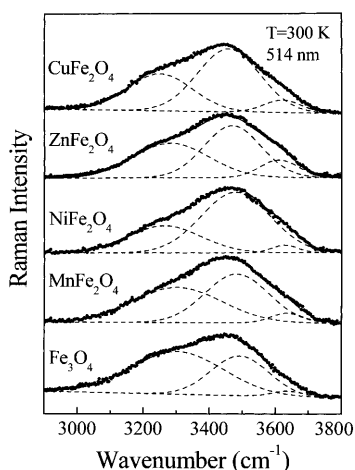


Fig. 3. Raman spectra of the UMF's in the OH stretching region. Symbols are experimental data, solid lines represent the best numerical fit, and dashed lines represent the gaussian-shaped Raman modes.

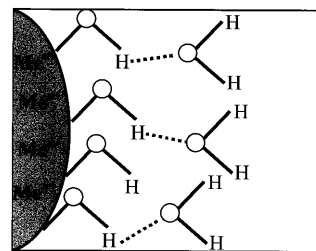


Fig. 4. Schematic representation of the nanoparticle surface of water-based UMF's. The chemisorbed OH-group is the Raman probe used in this work.

samples are dominated by the OH-groups chemisorbed at the nanoparticle surface. Stabilization of metal-oxide solid surfaces in contact with aqueous media, involving chemisorption of OH-groups at the metal-ion sites, is well known. Further, the high band gap oxide-semiconductor nanoparticle dispersed in the dielectric carrier liquid works as highly efficient scattering centers for visible light. Therefore, water molecules themselves, either close to or far away from the magnetic surface nanoparticle, do not scatter as much the incident laser light as the chemisorbed OH-group at the nanoparticle surface. Furthermore, the suppression of all symmetric OH stretching Raman modes from the UMF's is an obvious consequence of the vibrational quenching effect due to the replacement of a hydrogen atom from water by the magnetic nanoparticle surface. Fig. 4 shows a schematic representation of the metal-oxide nanoparticle surface in aqueous media, where the surface metal ions ( $\text{Me}^{n+}$ ) are meant to replace one hydrogen atom from the first molecular water layer. From the model picture displayed in Fig. 4, we claim that the hydroxyl Raman modes we are focusing our investigation correspond to the OH-group firmly bonded to the nanoparticle surface. In addition, the hydrogen bonding Raman modes are due to the hydrogen bonding established between the surface OH-group ( $\text{Me}^{n+} - \text{OH}$ ) and the first water molecular layer from the medium ( $\text{Me}^{n+} - \text{OH} \cdots \text{O}$ ).

Fig. 5 shows the Raman shift of the OH bending modes ( $\nu_2$  and  $\nu'_2$ ) of the UMF samples with respect to the values obtained from liquid water ( $1545$  and  $1643\text{ cm}^{-1}$ , respectively) versus the enthalpy change ( $\Delta H$ ) associated to the UMF samples containing different metals (Cu, Zn, Ni, and Fe). Symbols in Fig. 5 represent experimental data while the solid and dashed lines represent the linear fit of the experimental points. The lines (solid and dashed) in Fig. 5 do not represent any model calculation but the general trend of the experimental data, i.e. the wavenumber downshift of the OH bending Raman modes, relative to liquid water, as the enthalpy change increases. Note that the non-hydrogen bonding mode (open circles) presents a lower Raman downshift when compared to the hydrogen-bonding

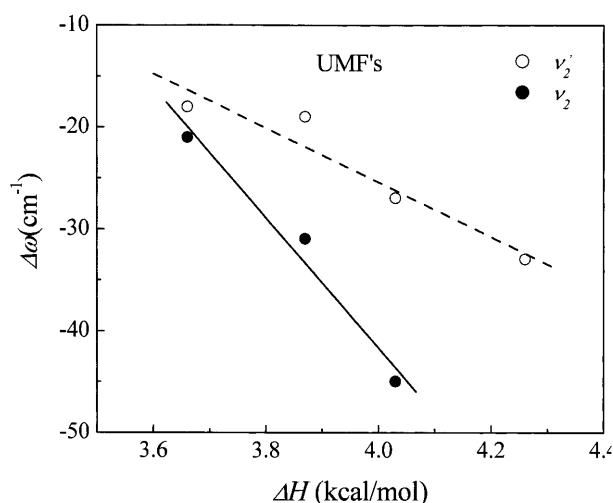


Fig. 5. Raman shift of the OH bending modes ( $\Delta\omega$ ) versus enthalpy change ( $\Delta H$ ) in the case of the UMF's. The vertical axis represent the Raman shifts with respect to the value found for liquid water (see Table 1).

mode (full circles). In fact, the slope associated to the dashed line in Fig. 5 is about half the slope of the solid line. Fig. 6 shows the Raman shift of the OH stretching modes ( $\nu_b$ ,  $\nu_d^a$  and  $\nu^a$ ) of the UMF samples, with respect to the values obtained from liquid water (3399, 3233, and 3628  $\text{cm}^{-1}$ , respectively), versus the enthalpy change ( $\Delta H$ ) associated to the UMF samples containing different metals (Cu, Zn, Ni, Mn, and Fe). Symbols in Fig. 6 represent experimental data while the solid and dashed lines represent the linear fit of the experimental points. Again, the lines (solid and dashed) in Fig. 6 do not represent any model calculation but the general trend of the experimental data, i.e., the wavenumber upshift of the OH stretching Raman

modes, relative to liquid water, as the enthalpy change increases. Note that the non-hydrogen bonding mode (open squares) presents a lower Raman wavenumber upshift when compared to the hydrogen bonding modes (full squares and full circles). Similarly to the case observed in the Raman bending modes the slope associated to the dashed line in Fig. 6 is about half the slope of the solid lines.

The main features observed in Fig. 5 and Fig. 6 may be qualitatively explained as follows. The higher Raman shift associated to the hydrogen bonding modes as a function of the enthalpy change is quite reasonable inside the harmonic oscillator picture, once the enthalpy change reflects directly (first order) the spring constant. The non-hydrogen bonding Raman modes would be influenced by the enthalpy change only marginally, through a second order coupling. Despite the differences in symmetry between bending and stretching Raman modes the slopes associated to the non-hydrogen bonding modes (see Fig. 5 and Fig. 6) are very much close to each other (about  $-30 \text{ mol/kcal} \times \text{mol}$ ). Likewise, the slopes associated to the bending and stretching hydrogen bonding modes (see Fig. 5 and Fig. 6) are about  $65 \text{ mol/kcal} \times \text{mol}$ . However, the slopes in Fig. 5 are negative while in Fig. 6 they are positive. The positive slope displayed in Fig. 6 may be understood partially once the spring constant associated to the hydrogen bonding increases as the enthalpy change increases, thus increasing the Raman frequency. In addition, a stronger interaction between the chemisorbed OH-group and the solvent would reduce the strength of the interaction of the chemisorbed OH-group and the nanoparticle itself, thus reflecting a wavenumber upshift. In other words, in the hydrogen bonding OH stretching mode the hydrogen atom displacement occurs parallel to the line connecting the three atoms involved ( $\text{O}-\text{H}^{\cdots}\text{O}$ ), which is the axis of the orbital describing the hydrogen bonding. The explanation of the negative slope displayed in Fig. 5, however, is subtler. In the hydrogen bonding OH bending mode the displacement of the hydrogen atom occurs perpendicularly to the line connecting the three atoms involved ( $\text{O}-\text{H}^{\cdots}\text{O}$ ), which is orthogonal to the axis of the orbital describing the hydrogen bonding and thus described through a perpendicular spring constant. Note that the higher the enthalpy change the stronger and more spatially localized the hydrogen bonding orbital along the line connecting the atoms involved ( $\text{O}-\text{H}^{\cdots}\text{O}$ ). Therefore, the perpendicular spring constant is expected to be very sensitive to the degree of spatial localization of the hydrogen bonding orbital. We argue that the perpendicular spring constant reduces as the degree of localization of the orbital increases. Such a picture partially explains, in qualitative grounds, the negative slope observed in Fig. 5. In addition, as the spring constant associated to the hy-

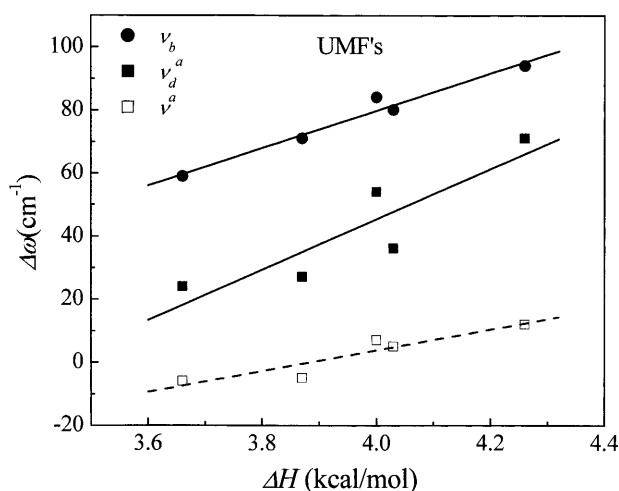


Fig. 6. Raman shift of the OH stretching modes ( $\Delta\omega$ ) versus enthalpy change ( $\Delta H$ ) in the case of the UMF's. The vertical axis represent the Raman shifts with respect to the value found for liquid water (see Table 1).

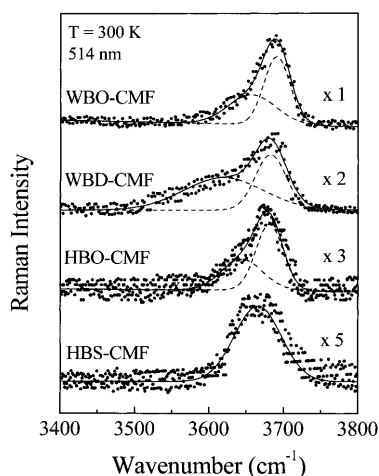


Fig. 7. Raman spectra of the CMF's in the OH stretching region. Symbols are experimental data, solid lines represent the best numerical fit, and dashed lines represent the gaussian-shaped Raman modes.

drogen bonding is reduced the chemisorbed OH-group is more available to interact with the nanoparticle surface, thus reducing the OH bending wavenumber.

### 3.3. Coated magnetic fluids

Hydrocarbon and water were used as the liquid carrier to yield stable magnetite-based CMF samples. The original hydrocarbon-based (HB-CMF) and water-based (WB-CMF) samples were diluted to about  $2 \times 10^{16}$  particle/cm<sup>3</sup>, in order to perform the Raman measurements. Dodecanoic acid was used as the first coating agent to produce the single coated hydrocarbon-based sample (HBS-CMF). Dodecanoic acid and an ethoxylated polyalcohol were used respectively as the first and the second coating agents to produce a double coated water-based sample (WBD-CMF). *N*-oleoylsarcosine was used as the first coating agent to produce two CMF samples. The first sample was dispersed in alkaline water (WBO-CMF) while the second sample was dispersed in hydrocarbon (HBO-CMF). The amino group of the *N*-oleoylsarcosine in the WBO-CMF sample is more likely to be linked to the nanoparticle surface, thus leaving the carboxyl group free to guarantee the water-based colloidal stability. On the other hand, when peptized in hydrocarbon, both functional groups (amino and carboxyl) may be used to bind to the nanoparticle surface and the colloidal stability in the HBO-CMF sample is achieved by the interaction of the non-polar chain of the coating molecule with the solvent. In the CMF's the Raman measurements were focused in the typical intra-molecular OH stretching mode region. Room temperature Raman spectra in the OH stretching mode region taken from all the CMF samples are shown in Fig. 7. From top to bottom, the Raman spectra in Fig. 7 correspond

to the WBO-CMF, WBD-CMF, HBO-CMF, and HBS-CMF samples, respectively.

In the WBO-CMF, WBD-CMF, and HBO-CMF spectra only two modes at the higher energy side of the Raman spectra ( $\nu_b$  and  $\nu_a$ ) were observed. The presence of only two Raman modes in these three samples, in comparison with both the five Raman modes observed in liquid water (Fig. 1) and the three Raman modes observed in the UMF's (Fig. 3), is partly explained as long as a vibrational quenching effect is assumed, similarly to the discussion presented in Section 3.2. Suppression of the  $\nu_a$  Raman mode from the CMF's is straightforward once the coating layer, which is chemisorbed at the nanoparticle surface, inhibits water molecules from the medium to bind to the OH-group at the nanoparticle surface. Therefore, the two Raman modes left behind in three of the CMF's (WBO-CMF, WBD-CMF, and HBO-CMF) are the anti-symmetric non-hydrogen bonding ( $\nu_a$ ) plus the anti-symmetric hydrogen bonding ( $\nu_b$ ). The quenching of an extra Raman mode ( $\nu_b$ ) from the HBS-CMF sample, however, is mainly attributed to the lack of hydrogen bonding between the residual OH-group chemisorbed at the nanoparticle surface and either the long carbon chain from the dodecanoic acid or from the non-polar solvent. Therefore, the only Raman mode left behind in the HBS-CMF sample is the asymmetric non-hydrogen bonding one ( $\nu_a$ ). Note that the possibility of a hydrogen bonding between the residual OH-group chemisorbed at the nanoparticle surface and the OH-group from the ethoxylated polyalcohol (or *N*-oleoylsarcosine) accounts for the presence of the  $\nu_b$  Raman mode in the WBO-CMF, WBD-CMF, and HBO-CMF samples.

From the fitting procedure it was found that the Raman lines in the WBO-CMF sample is more intense than the same Raman lines in the other three CMF samples, reaching five times the intensity found in the HBS-CBF sample (see numbers in Fig. 7). The intensity reduction of the Raman lines is a clear indication of the reduction of the hydroxyl-grafting coefficient ( $\xi$ ) in the following order:  $\xi$  (WBO-CMF) >  $\xi$  (WBD-CMF) >  $\xi$  (HBO-CMF) >  $\xi$  (HBS-CMF). In fact, the intensity reduction of the OH stretching Raman modes in the HB-CMF samples with respect to the WB-CMF samples reflects the reduction of the surface-grafting coefficient associated to the OH-group ( $\xi$ ). This is an expected behavior, once in the WBO-CMF one functional group of the *N*-oleoylsarcosine molecule is used to bind to the nanoparticle surface while the other functional group is left free to interact with the polar solvent (water). Therefore, more metal sites are available at the nanoparticle surface for the chemisorbed OH-groups. Nevertheless, the grafting coefficient associated to each one of the functional groups (amino and carboxyl) is still an open question. In contrast, in the



HBO-CMF the two functional groups of the *N*-oleoylsarcosine are linked to the nanoparticle surface, thus resulting in a reduction of the OH-grafting coefficient. Note that the reduction of the *N*-oleoylsarcosine grafting in the WBO-CMF with respect to the HBO-CMF is indirectly obtained through the increasing of the OH-grafting coefficient in the WBO-CMF with respect to the HBO-CMF. Comparison of the OH stretching Raman intensity (*I*) between the WBO-CMF and the WBD-CMF samples leads approximately to  $I(\text{WBD-CMF})/I(\text{WBO-CMF}) \approx 0.5$ . Such an intensity reduction can be explained considering that the double layer (dodecanoic acid plus ethoxylated polyalcohol) is more efficient in keeping the water molecules of the solvent far from the nanoparticle surface, thus resulting in a reduction of the OH-grafting coefficient of the WBD-CMF sample with respect to the WBO-CMF sample. In the case of the HBS-CMF sample, the OH-grafting coefficient is extremely reduced, for neither OH-groups are present in the coating layer nor water molecules are found in the solvent to help stabilize, via hydrogen bonding, OH-groups bonded to the nanoparticle surface. It is important to remind that the presence of OH-groups in the HBS-CMF sample is explained as coming from the nanoparticle synthesis process, which is performed in alkaline aqueous medium. A quantitative description of all the issues discussed above, however, require further experimental and theoretical investigations.

Table 1 presents the main parameters resulting from the gaussian fit of the Raman spectra associated to the OH-group. Table 1 includes the Raman data taken from liquid water (first line), used in this work to study the shift in wavenumber of the corresponding Raman modes in both the UMF and CMF samples. From the data shown in Table 1 the wavenumber upshift of the  $\nu^a$  Raman mode in the WBO-CMF ( $63 \text{ cm}^{-1}$ ) with respect to the liquid water is smaller than the observed in the case of the  $\nu_b$  Raman mode ( $259 \text{ cm}^{-1}$ ). Furthermore, the enthalpy change associated to the WBO-CMF is smaller than the value found in liquid water. These data show that in the WBO-CMF sample the OH-group at the nanoparticle surface has a weaker interaction with the surrounding medium (solvent and/or coating). Similar wavenumber upshift and enthalpy change is observed in all the CMF samples. Note that the Raman intensity of the hydrogen bonding Raman modes with respect to the non-hydrogen bonding Raman modes indicate more efficiently the interaction established between the OH-group chemisorbed at the nanoparticle surface and the surrounding medium, through the value of the enthalpy change. Finally, in the UMF the enthalpy change is above the value found in liquid water, while in the

CMF the enthalpy change is below the value found in liquid water.

#### 4. Conclusions

In summary, the usefulness of the Raman spectroscopy in the study of UMF's and CMF's is fully demonstrated in this work. In particular, Raman spectroscopy would be used as a powerful technique to investigate the microscopic details of the first molecular layer about the nanoparticle surface, i.e. the interface nanoparticle surface-carrier liquid or the interface nanoparticle surface-coating layer. In the UMF's based on different spinel ferrites (Cu, Zn, Ni, Mn, and Fe), it was found that the quenching of the symmetric OH stretching modes from the Raman spectra is a general trend, indicating that chemisorbed OH-groups at the nanoparticle surface dominate the light scattering process. In comparison to the UMF's the CMF's analyzed in this work present an extra reduction of one stretching Raman mode ( $\nu_d^a$ ) for three samples (WBO-CMF, WBD-CMF, and HBO-CMF) and an extra reduction of two stretching Raman modes ( $\nu_d^a$  and  $\nu_b$ ) for one sample (HBS-CMF). Such an extra quenching of the stretching Raman modes was explained in terms of the interaction between the chemisorbed OH-group and both the coating layer and the solvent. The wavenumber upshift observed in the three OH stretching modes ( $\nu_d^a$ ,  $\nu_b$ , and  $\nu^a$ ) of the UMF samples reflects a weaker interaction between the OH-group at the nanoparticle surface and the nanoparticle surface itself. However, the increase of the enthalpy change observed in the UMF samples with respect to the liquid water indicates a stronger interaction between the OH-group at the nanoparticle surface and the solvent. However, the wavenumber downshift versus the enthalpy change, observed in the two OH bending modes ( $\nu_2$  and  $\nu_2'$ ) of the UMF samples, reflect a stronger interaction between the OH-group at the nanoparticle surface and the nanoparticle surface itself. Indeed, the use of the chemisorbed OH-group to probe the degree of grafting of different coating agents was successfully performed using Raman spectroscopy. It was found that the *N*-oleoylsarcosine-grafting coefficient in the HBO-CMF sample is about three times the *N*-oleoylsarcosine-grafting coefficient in the WBO-CMF sample. The highest grafting coefficient associated to the coating agent was achieved in the case of the HBS-CMF sample.

#### Acknowledgements

This work was partially supported by the Brazilian agencies CNPq, FAP-DF, PADCT, and CAPES.

## References

- [1] Berkovsky BM, Mecerdev VF, Krakov MS. *Magnetic Fluids: Engineering Applications*. New York: Oxford University Press, 1993.
- [2] Massart R. *IEEE Trans Mag* 1981;17:1247–8.
- [3] Fanyao Q, Morais PC. *J Chem Phys* 1999;111:8588–94.
- [4] Rosensweig RE. *Ferrohydrodynamics*. New York: Cambridge University Press, 1985.
- [5] Lacava ZGM, Azevedo RB, Lacava LM, Martins EV, Garcia VAP, Rébola CA, et al. *J Mag Mag Mater* 1999;194:90–5.
- [6] Lacava ZGM, Azevedo RB, Martins EV, Lacava LM, Freitas MLL, Garcia VAP, et al. *J Mag Mag Mater* 1999;201:431–4.
- [7] Halbreich A, Roger J, Pons J-N, Da Silva MF, Hasmonay E, et al. In: Schutt W, Teller J, Häfeli U, Zborowski M, editors. *Scientific and Clinical Applications of Magnetic Carriers*. New York: Plenum Press, 1997:399–412.
- [8] Hermetin P, Doenges R, Franssen V, Bieva C, Bruggen FJV. *Bioconjug Chem* 1990;1:411–5.
- [9] Kuznetsov A, Filippov VI, Kuznetsov OA, Gerlivanov VG, Dobrinsky EK, Malashin SI. *J Mag Mater* 1999;194:22–30.
- [10] Jung CW, Rogers JM, Groman EV. *J Magn Magn Mater* 1999;194:210–6.
- [11] Jordan A, Scholz R, Wust P, Fhlingm H, Felix H. *J Mag Mag Mater* 1999;201:413–9.
- [12] Garbassi F, Morra M, Occhiello E. *Polymer Surfaces: From Physics to Technology*. New York: John Wiley, 1998.
- [13] Tourinho FA, Franck R, Massart R. *J Mater Sci* 1990;25:3249–54.
- [14] Cullity BD. *Introduction to Magnetic Materials*. Reading, MA: Addison-Wesley, 1972.
- [15] Wilson SR, Ridler PJ, Jennings BR. *J Phys D: Appl Phys* 1996;29:885–8.
- [16] Davies HW, Llewellyn JP. *J Phys D: Appl Phys* 1979;12:311–9.
- [17] Tronconi AL, Morais PC, Pelegrini F, Tourinho FA. *J Magn Magn Mater* 1993;122:90–2.
- [18] Bakuzis AF, Morais PC, Tourinho FA. *J Magn Reson A* 1996;122:100–3.
- [19] Silva GJ, Morais PC, Tourinho FA. *J Phys Chem* 1996;100:14269–71.
- [20] Morais PC, Lara MCFL, Tronconi AL, Tourinho FA, Pereira AR, Pelegrini F. *J Appl Phys* 1996;79:7931–5.
- [21] Morais PC, Tourinho FA, Gonçalves GRR, Tronconi AL. *J Mag Mag Mater* 1995;149:19–21.
- [22] Bakuzis AF, Morais PC, Pelegrini F. *J Appl Phys* 1999;85:7480–2.
- [23] Silva GJ, Morais PC, Tourinho FA. *J Chem Phys* 1997;107:2793–7.
- [24] Morais PC, daSilva SW, Soler MAG, Sousa MH, Tourinho FA. *J Mag Mag Mater* 1999;201:105–9.
- [25] Morais PC, daSilva SW, Soler MAG, Buske N. *J Phys Chem A* 2000;104:2894–6.
- [26] Gunther D, Buske N. DE patent 1993; 4325386.
- [27] Scherer JR, Go MK, Kint S. *J Phys Chem* 1974;78:1304–13.
- [28] Carey DM, Korenowski GM. *J Chem Phys* 1998;108:2669–75.
- [29] Walrafen GE. *J Chem Phys* 1964;85:3246–50.
- [30] Walrafen GE, Fisher MR, Hokmabadi MS, Wang W-H. *J Chem Phys* 1986;85:6970–5.
- [31] Walrafen GE, Blatz LA. *J Chem Phys* 1973;59:2646–51.